Response to Referee#2

We thank the referee for the careful assessment of our manuscript and for the constructive comments on the receiver characterization, calibration procedures, retrieval performance, and uncertainty assessment.

Comment 1)

Lines 13–16: The authors statement "To overcome this limitation" is not completely valid because the described approach only partially addresses the signal contamination problem by Mie scattering. In this manuscript the temperature retrievals are limited to 5.3 km and above. Please rephrase the statement to indicate that the technique partially addresses the contamination problem.

Response:

We agree that the original wording was not sufficiently precise. Resolving the atmospheric spectrum provides information for distinguishing molecular and particle scattering, but it does not eliminate the influence of Mie scattering on temperature retrieval. These revisions have been made in the Abstract on Page 1, Lines 13–18 and 24–26, and Page 2, Lines 54–62.

Comment 2)

Line 45: An alternative approach for atmospheric temperature profiling that is immune to contamination by Mie scattering is based on iodine-vapor-filter HSRL. Please consider referring to this alternative approach and cite the relevant work by Hair et al., "High-Spectral-Resolution Lidar with Iodine-Vapor Filters: Measurement of Atmospheric-State and Aerosol Profiles," Applied Optics, 40, 5280–5294 (2001).

Response:

Thank you for suggesting this relevant reference. We have added Hair et al. (2001) to the Introduction and acknowledge iodine-vapor-filter HSRL as an alternative approach for atmospheric-state profiling and molecular–particle discrimination. The corresponding text has been added on Page 3, Lines 72–73.

Comment 3)

Line 176 and Fig. 2(a): The authors state that the instrument has a coaxial transmitter–receiver configuration. However, the conceptual image shows a biaxial arrangement of the instrument. The biaxial configuration would explain the lower 2km blind zone that is not discussed in the manuscript. Please clarify the instrument configuration.

Response:

Thank you for pointing out this inconsistency. The original description of the transmitter–receiver configuration was incorrect and has been corrected in the revised manuscript (Page 8, Line 181).

Comment 4)

Line 178: It is likely that the instrument's hardware components such as wavelength meter as well as the laser frequency locking scheme and frequency long term stability were previously described in earlier papers. However, it would be valuable to either provide more detailed hardware description in this manuscript or to refer to the previously published paper that includes more details.

Response:

Thank you for this suggestion. We have expanded the hardware description to specify the wavelength meter and seed laser models and clarify the frequency-stabilization scheme. A small fraction of the transmitted 355 nm beam is monitored by a wavelength meter (HighFinesse, WS8-2), and the measured wavelength is fed to a custom-built PID controller for feedback control of the 1064 nm seed laser (NKT Photonics, K8230). These details have been added on Page 8, Lines 181–184.

Comment 5)

Line 185: Please consider specifying the manufacturer and model number of the linear PMT array.

Response:

Thank you for this suggestion. We have added the manufacturer and model of the linear

PMT array (Hamamatsu, H11460-200) to the revised manuscript (Page 11, Line 266).

Comment 6)

Equation (12): Equation 12 estimates the number of the photons detected by each channel. Assuming the convolution with the transmission function of the receiver accounts for the fraction of the N total photons in each channel, dividing N(z) received photons by N number of channels can be a duplicate in normalization. Please clarify the normalization in the Equation 12.

Response:

Thank you for pointing out this ambiguity. We have revised Eq. (13) to explicitly integrate the convolved spectral response over the effective width of each detector channel. Under the stated ideal assumptions, $N(z)/\mathrm{L_{if}}$ represents the spatially uniform incident count density, while the convolved response accounts for the frequency-dependent transmission of the Fizeau interferometer. We have also clarified that the combined molecular and Mie spectrum is normalized to unit area. This formulation replaces the original division by the number of channels and clarifies the normalization (Lines 233–242). The revised Eq. (13) is shown below.

$$N_j(y_j, \nu, z, T) = \frac{N(z)}{\mathrm{L_{if}}} \cdot \int_{y_j-\Delta y/2}^{y_j+\Delta y/2} \{[S_{rb}(\nu, z, T) + S_{Mie}(\nu)] \otimes F(\nu - \nu(y)) \otimes S_{laser}(\nu)\}\, dy$$

Comment 7)

Line 230: Please revise the terminology regarding returns and detector counts: “the total number of returned photons”. The dark counts do not contribute to the “returned photons” since they do not originate from the returned photons, but rather contribute to the total number of counts. Please distinguish consistently between “returned photons” and total number of counts.

Response:

Thank you for pointing out this terminology issue. We have replaced “the total number of returned photons” with “the total expected counts” to distinguish the atmospheric return from detector dark counts and background counts (Line 239).

Comment 8)

Lines 240–250: The optimization problem is a trade-off due practical constraints and often does not have a single optimal solution. According to the presented metric shown in Figure 3, the optimum detector channel number appears to be 16. However, the performance is not significantly different between cases for 8 and 128 channels provided the proposed metric has an offset of only 1km. Intuitively, with increasing number of detectors the dark counts start to dominate the returns and degrade SNR. The opposite is true for decreasing number of detectors. What is the minimum number of spectral bands are required for the accurate measurements? The presented color map shown in the Figure 3 has a vertical resolution of 1 km. Later in the manuscript the profile retrievals use coarse 300 m vertical resolution above 10km. It is unclear whether the calculations demonstrated in Figure 3 are accounting for larger vertical integration above 10 km or authors use 1km vertical resolution in the modeling. Please clarify.

Response:

Thank you for this valuable comment. Your insightful suggestions prompted us to reconsider our approach to optimizing the number of detector channels and to conduct a more comprehensive and realistic numerical simulation. In the revised simulation, we adopted the same vertical resolution as that used in the atmospheric measurements, with 60 m below 10 km and 300 m above 10 km. Furthermore, we directly evaluated the performance of different channel configurations at each altitude using the root mean square errors (RMSEs) of the retrieved temperature and wind velocity. Seven detector configurations with 4, 8, 16, 32, 64, 128, and 256 channels were investigated in the revised simulations.

Hagen et al. examined the effects of sampling density, finite pixel width, and noise on the estimation of Gaussian spectral parameters, highlighting the importance of balancing spectral sampling resolution and measurement uncertainty (Hagen et al., 2007). Our retrieval method is based on spectral fitting and involves four free parameters. Therefore, at least four spectrally independent measurements are required for parameter estimation, making four channels the theoretical minimum for our

retrieval approach. Furthermore, our simulation results demonstrate that the four-channel configuration can also achieve relatively good retrieval accuracy. Increasing the number of channels provides only limited improvement in retrieval accuracy, while configurations with larger numbers of channels may even exhibit degraded performance due to reduced signal-to-noise ratios (SNRs), as illustrated in the revised Fig. 3. Ultimately, the 32-channel configuration was selected as a compromise among overall system robustness, complexity, and the commercial availability of multichannel PMT arrays. The revised Fig. 3 is shown here as Fig. R1.

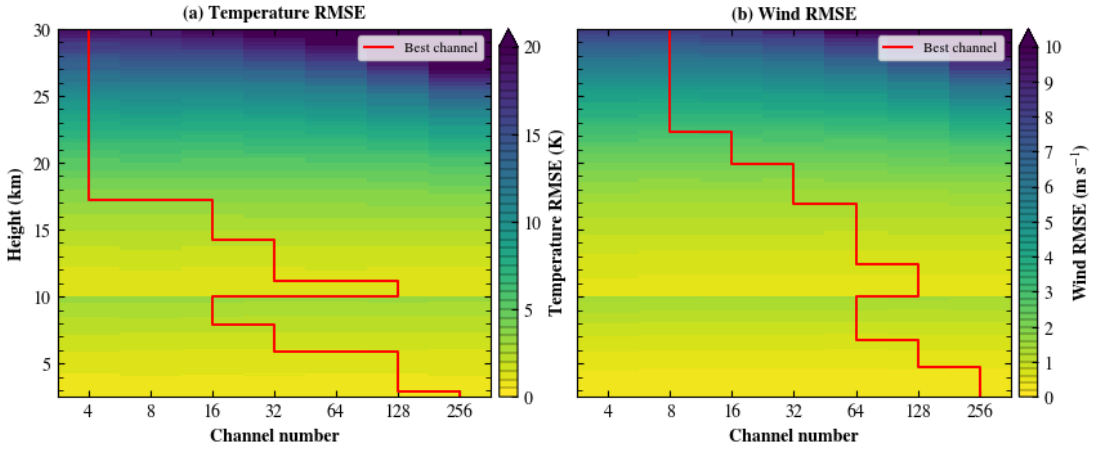


Figure R1. Influence of detector channel number and detection height on the retrieval accuracy of (a) temperature and (b) wind velocity.

The corresponding revisions can be found on Pages 10–11, Lines 244–267.

Comment 9)

Section 4, Fig. 5: The authors show a rapid convergence of their retrieval algorithms demonstrating a mean error across the altitudes 2-4 km and 5-20 km. Please explain how the algorithm is converging within single cycle independent of the amplitude of the original perturbation and whether it demonstrates the same convergence rate when multiple parameters are perturbed. Convergence of the mean error of the retrieval do not represent the convergence of retrievals at individual altitudes. Assuming Figure 6 represents the converged result of the same simulation, it then demonstrates the

resulting biases of the retrievals at individual altitude rather than the mean error of the profile. It would be more indicative of the successful convergence if the authors can demonstrate the convergence for individual retrievals.

Response:

Thank you for this valuable comment. Your observations are well-founded and have prompted us to conduct a more comprehensive analysis of the convergence behavior of our retrieval algorithm. In response to your suggestions, we performed a new set of numerical simulations using a vertical resolution of 60 m below 10 km and 300 m above 10 km. Furthermore, we systematically investigated the convergence behavior of the temperature and wind velocity retrievals at individual altitudes, the effects of simultaneous deviations in the initial guesses of multiple parameters, and the resulting retrieval accuracy.

First, we would like to clarify that our retrieval algorithm does not converge within a single iteration. When the initial guesses deviate substantially from the true parameter values, the first iteration may produce a relatively large reduction in retrieval errors; however, several additional iterations are still required to achieve convergence. Furthermore, larger deviations in the initial guesses generally require more iterations for both temperature and wind velocity retrievals to converge compared with smaller initial deviations. To demonstrate this behavior, we selected a representative case from our numerical simulations, as shown in Fig. R2.

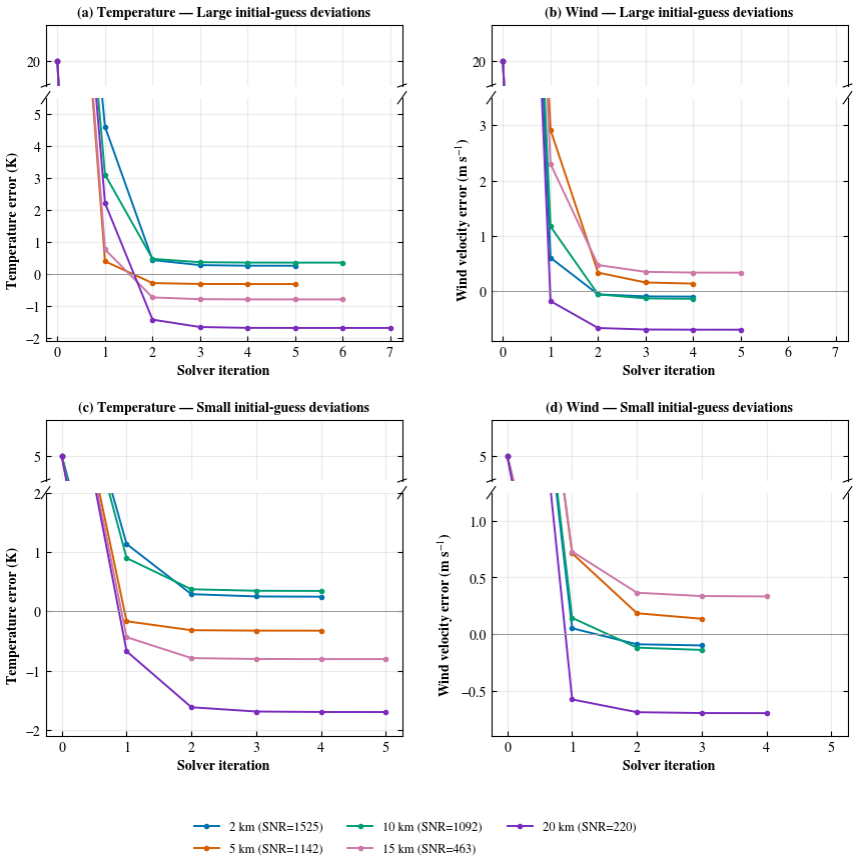


Figure R2. Convergence of temperature and wind velocity retrieval errors at five heights for the first Monte Carlo realization. Iteration 0 denotes initialization.

Figure R2 illustrates the convergence of the first of the 100 Monte Carlo realizations as an example. The plotted cases included small initial-guess deviations (temperature: +5 K; wind velocity: +5 m s^{-1}; RB amplitude: +20 %; Mie amplitude: −20%) and large initial-guess deviations (temperature: +20 K; wind velocity: +20 m s^{-1}; RB amplitude: +50%; Mie amplitude: −50%), applied simultaneously to the initial values of all four parameters. The temperature and wind velocity retrievals stabilize within a few solver iterations at all five heights. Larger initial-guess deviations generally require more iterations.

The revised Fig. 5 presents the altitude-dependent mean number of iterations required for temperature and wind velocity retrievals to converge under different initial-guess deviations, based on 100 simulation runs. It also shows the RMSEs of the retrieved temperature and wind velocity for different initial-guess deviations. The results demonstrate that the retrieval algorithm achieves convergence at all investigated

altitudes, with nearly identical converged values across different initial guesses. Although larger initial-guess deviations generally increase the number of iterations required for convergence, they have a negligible influence on the final retrieval accuracy. The revised Fig. 5 is shown here as Fig. R3.

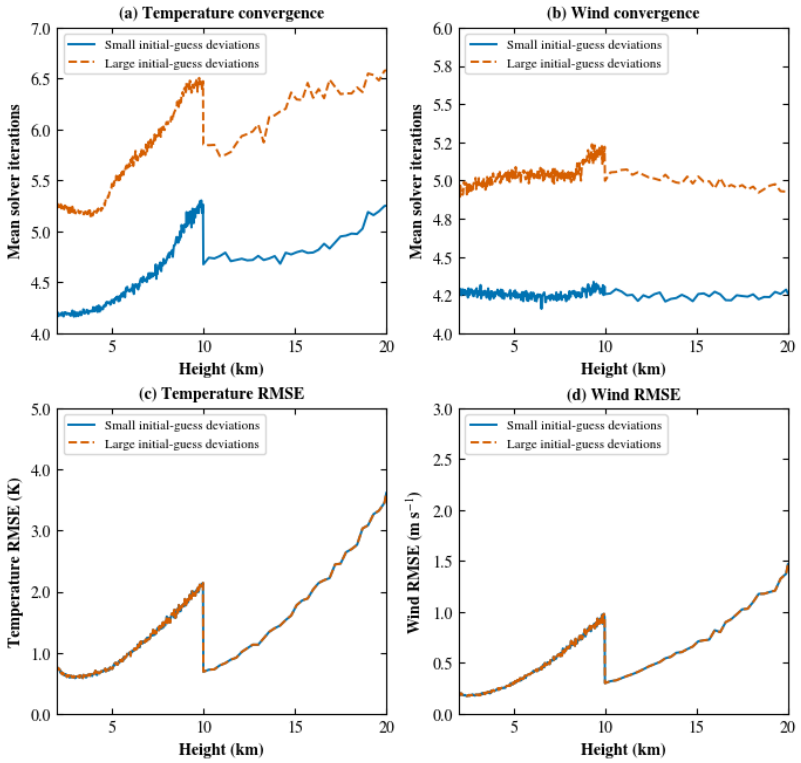


Figure R3. Comparison of mean solver iteration counts for (a) temperature and (b) wind velocity retrievals, and RMSEs of (c) temperature and (d) wind velocity.

The corresponding revisions can be found on pages 13–14, lines 305–331 of the revised manuscript.

Comment 10)

Fig 6, lines 285–289: The authors state “As shown in Fig. 6, the retrieved temperature exhibits a noticeable negative bias between 2 and 4 km. This underestimation is mainly caused by the increasing contribution of Mie scattering in the lower troposphere.” However, authors do not explain an introduced contamination by Mie signal for the presented modeling result. In my opinion, the temperature retrieval bias profile shown in Figure 6(a) experience a positive linear trend below 5km. This is hard to attribute it

to an existence of such aerosol gradient in the lower atmosphere up to 5km. Please, provide an explanation on the mechanism that causes this bias or explain the modeling process if aerosol profile was used in the model to intentionally introduce the bias.

Response:

We thank the reviewer for questioning our previous interpretation. Upon re-examining the retrieval implementation, we identified an inappropriate bound on the Mie intensity parameter that restricted its adjustment during the fitting. Because temperature and Mie intensity are coupled, this restriction caused the temperature estimate to compensate, resulting in an underestimation. The previously reported bias therefore arose from the parameter constraint in the retrieval implementation, rather than from the prescribed aerosol profile itself.

We have corrected this constraint and repeated the simulations and retrievals. We also revised the simulation range resolution to match that used in the actual observations: 60 m below 10 km and 300 m above 10 km. The updated results, now presented in Fig. 6, no longer show the previously reported systematic temperature underestimation in the lower-height region. We have consequently removed the statement attributing that bias to an increasing Mie contribution. Appendix A has also been added to document the simulation settings, atmospheric profiles, and representative simulated signals.

The corresponding revisions can be found on pages 13–14, lines 294–306 of the revised manuscript. Appendix A is provided on page 24. The revised Fig. 6 is shown here as Fig. R4.

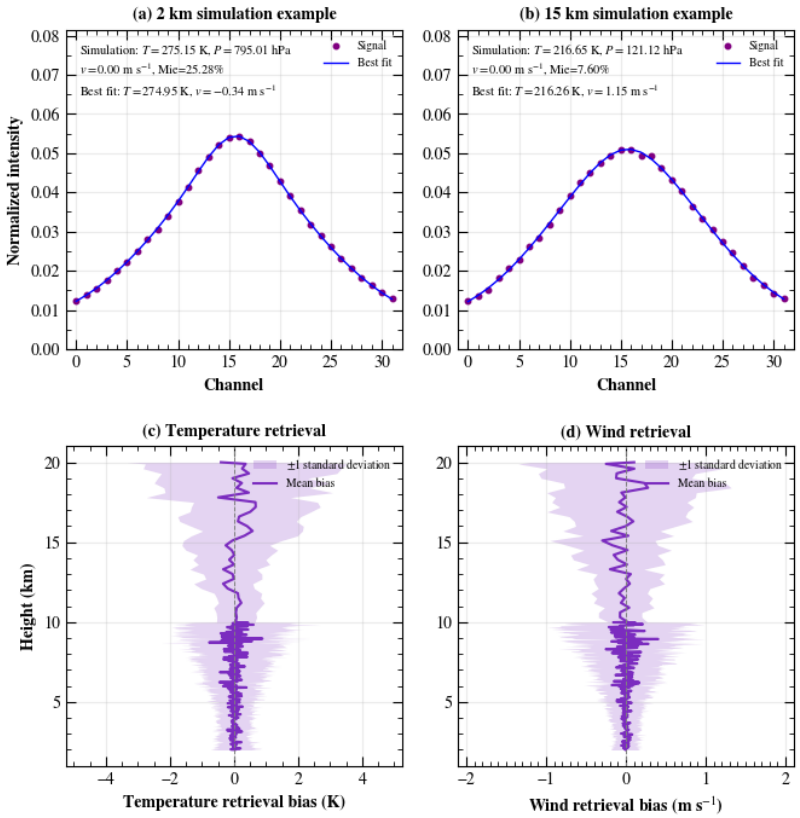


Figure R4. Examples of normalized simulated photon counts and their best fits at (a) 2 km and (b) 15 km. Mean retrieval biases and standard deviations of (c) temperature and (d) wind velocity as functions of height.

Comment 11)

Fig 8(a–c): The authors report the measured and the fitted spectra at 4.5, 4.6, and 4.7 km with changing contribution of Mie scattering. Based on the width of the Mie peak in the modeled spectra, the fitted curve represents a model of RB + Mie spectra not convoluted with the instrument function (laser spectra and receiver's transmission function). However, the authors comparing the calculated RB spectra with the measured one. Please explain the purpose of such comparison. In my opinion, the shape of the measured curves is asymmetric and visually would not be even closely matching the fitted curve once it is convoluted with the measured transmission functions and laser spectrum from Figure 7. The fitted curves have narrow peak from Mie scattering that does not appear in the measured signals even at 4.5 km. I believe, the asymmetry in the

measured spectra is indicative of the asymmetry in the receiver's transmission function. For reference, Figure 7 shows a measured receiver's transmission functions in the laboratory setting with a much smaller skewness. I assume that field measured spectra are affected by the difference in illumination of the Fizeau vs in the laboratory setting, or less likely by possible etalon/Fizeau drift. Please explain such large discrepancy in the two spectra and describe the correction procedure of the transmission function that allows to achieve such a good accuracy for the temperature profile above 5.3 km. Also, the lidar temperature profiles presented in the Figure 8 do not appear to have a native resolution of 60 m below 10 km and 300 m above 10 km. Please specify what type smoothing was applied to the profile and present an unsmoothed version of the lidar temperature profile.

Response:

Thank you for this valuable comment. We first acknowledge an error in the original calculation of the Mie scattering fraction. After correcting this calculation, the retrieved Mie fractions were higher than those reported in the previous version of the manuscript. We have updated the corresponding results and discussion accordingly.

We would also like to clarify the purpose of presenting the spectra in Fig. 8(a–c). Our retrieval algorithm can reconstruct the atmospheric backscattered spectrum, including both Rayleigh–Brillouin (RB) and Mie scattering components. These spectra were originally presented to illustrate how different Mie scattering contributions affect the spectral shape. In the revised figure, we have removed the atmospheric scattering spectra obtained by deconvolution and instead present the best-fit results alongside the measured signals, allowing a direct comparison in the measurement domain. To further illustrate the influence of Mie scattering on the spectral shape, we have replaced the examples with results at heights of 4, 4.7, and 6 km, representing different Mie scattering contributions. The revised Fig. 10 is shown here as Fig. R5.

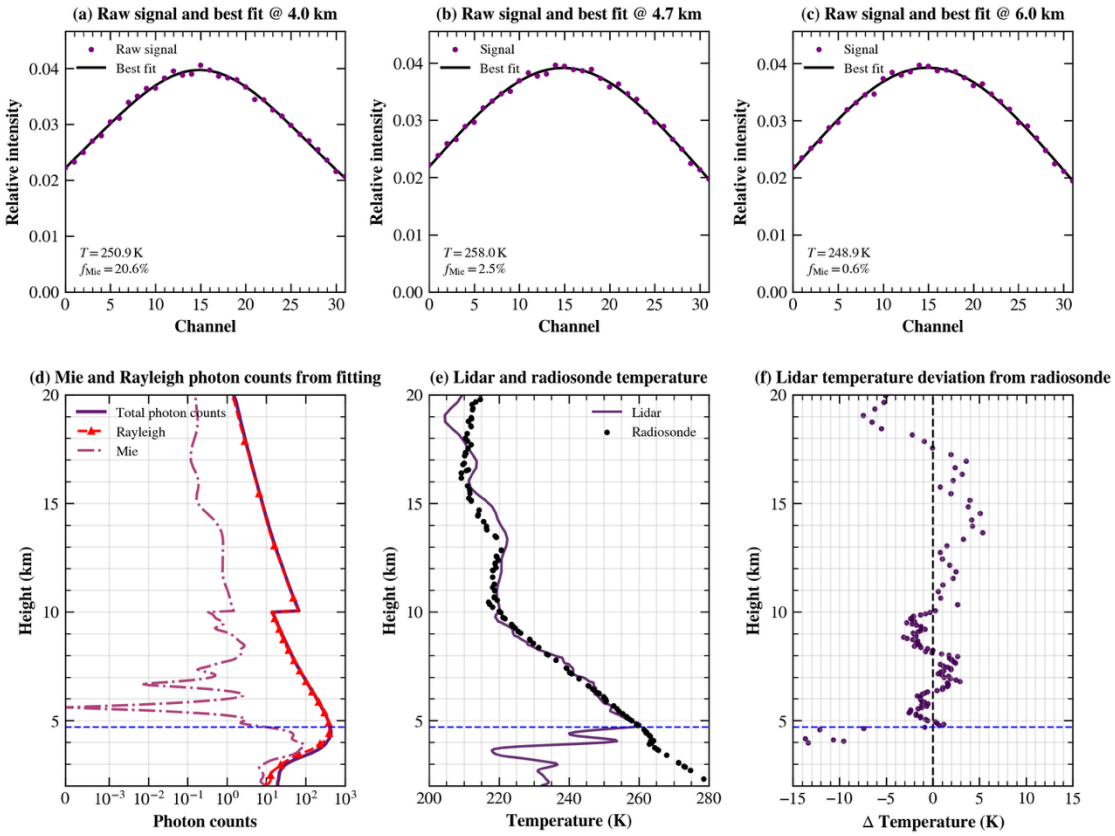


Figure R5. Spectral fitting results and evaluation of the influence of Mie scattering on temperature retrieval. (a–c) Best-fitting results of the measured signals at 4.0, 4.7, and 6.0 km. (d) Retrieved total, RB, and Mie photon counts. (e) Comparison between the lidar-retrieved and radiosonde temperature profiles. (f) Temperature difference (lidar minus radiosonde). The blue dashed line indicates the lower boundary of the temperature retrieval (4.7 km).

Regarding the reviewer's concern about why the narrow Mie scattering peak is not clearly observed in the measured spectra, we would like to clarify that the molecular (Rayleigh–Brillouin) and aerosol (Mie) scattering components are superimposed in the measured spectrum. Due to the finite spectral resolution of the Fizeau interferometer, the intrinsically narrow Mie scattering component is significantly broadened after convolution with the instrument response function. Consequently, the Mie scattering contribution affects the overall spectral shape rather than appearing as a distinct narrow peak.

To further demonstrate this effect, we performed additional simulations based on Eq. (13) of the manuscript. The ideal measurement spectra were calculated for four different Mie scattering fractions: 15%, 10%, 5%, and 0%. These simulations illustrate how the

narrow Mie scattering component is broadened by the instrument response and superimposed on the broader Rayleigh–Brillouin spectrum, thereby modifying the overall measured spectral shape without producing a clearly distinguishable narrow peak. The simulation results are presented in Fig. R6.

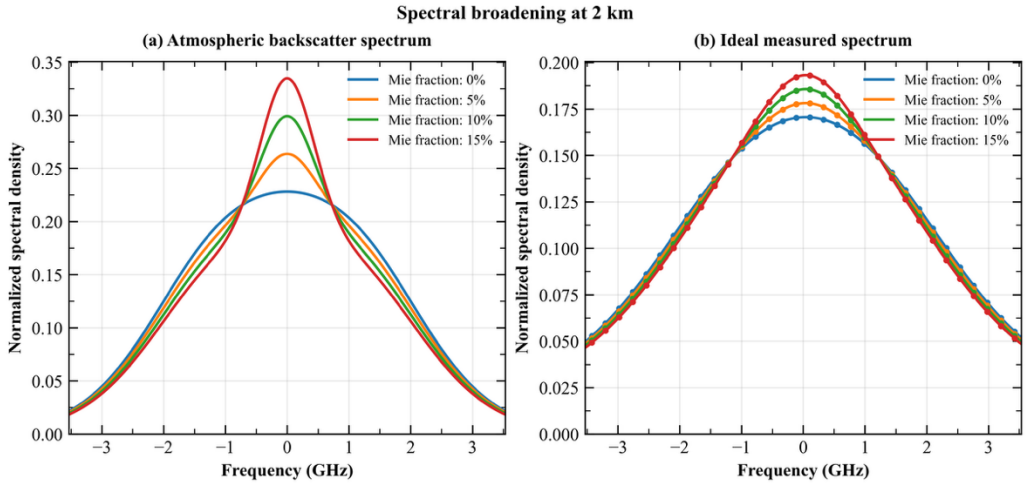


Figure R6. (a) Atmospheric backscatter spectra broadened by the laser linewidth and (b) ideal responses after transmission through the Fizeau interferometer at 2 km for Mie fractions of 0%, 5%, 10%, and 15%.

We apologize for the confusion caused by the presentation of the measured spectra. We would like to clarify that the spectra shown in the figure represent the raw photon counts recorded by the photon-counting acquisition system, without correction for the illumination function of the 32-channel PMT array. The nonuniform illumination across the detector channels can contribute to the apparent asymmetry of the measured spectra. To address this issue, we have added a detailed description of the illumination function calibration and correction procedure in the revised manuscript (Page 15, Lines 309–318). The added Fig. 7 is shown here as Fig. R7.

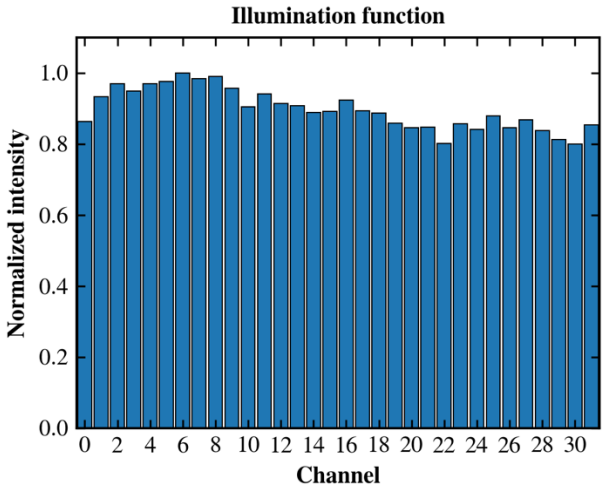


Figure R7. Illumination function of the 32-channel PMT array.

Furthermore, we have replaced the originally presented spectra with the illumination-function-corrected photon-counting signals and included the corresponding best-fit curves for comparison. The revised results are shown in Fig. R5

Regarding the reviewer's concern about the apparent inconsistency in the vertical resolution of the temperature profiles, we would like to clarify that the temperature profiles presented in the original manuscript were smoothed using a Gaussian filter with a standard deviation of $\sigma = 1.5$ data points to reduce small-scale fluctuations and better illustrate the overall vertical temperature structure.

In Fig. R8, we present the original unsmoothed temperature profile and the corresponding Gaussian-smoothed temperature profile based on the data shown in the Fig. R5(e).

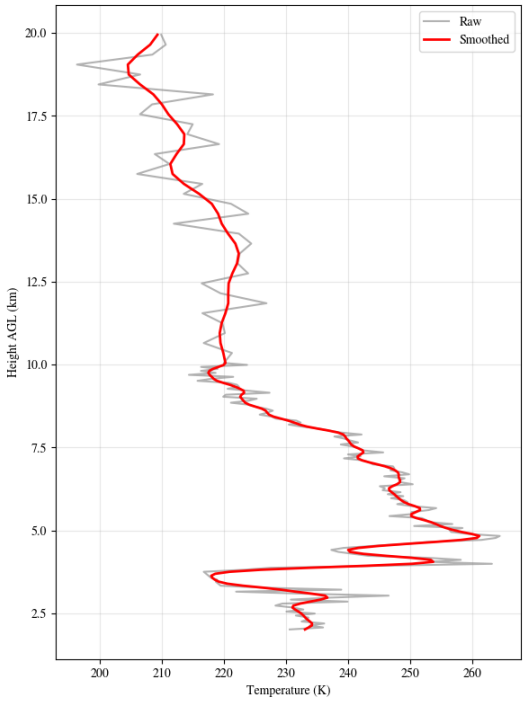


Figure R8. Comparison of the original unsmoothed temperature profile (Raw) and the Gaussian-smoothed temperature profile (Smoothed, σ = 1.5 data points) corresponding to Fig. R5(e).

Comment 12)

Table 1: Please include in the table 1 more technical parameters of the hardware: the laser manufacturer and model, frequency-locking accuracy, and long-term frequency drift as these are important parameters for reliable operation. Table 1 contains the duplicated "Transceiver" headings. Please replace them with "Transmitter" and "Receiver" where appropriate. Later in the manuscript authors report the laser linewidth of 0.67 GHz, while in the table the specified value is "<1GHz". Consider replacing it with more accurate value of 0.67GHz. Please also clarify what optical components "optical efficiency" parameter accounts for.

Response:

Thank you for this valuable comment. We have revised the manuscript to provide additional technical details regarding the laser system. Specifically, the manufacturer and model information of the laser system have been added on Page 7, Lines 174–180.

In addition, the frequency-locking accuracy has been included in Table 1 of the revised manuscript to provide a more comprehensive description of the laser's frequency stability performance. We have also replaced the duplicated “Transceiver” headings with “Transmitter” and “Receiver” and updated the laser linewidth to approximately 0.67 GHz.

Regarding long-term frequency drift, our laser system employs an active frequency-locking module to suppress frequency variations during operation. During the 46-minute monitoring period, no clear monotonic trend was observed in the measured laser frequency, and the standard deviation of the frequency fluctuations was 5.26 MHz as shown in Figure R9. These results indicate that frequency drift was limited over the monitored period.

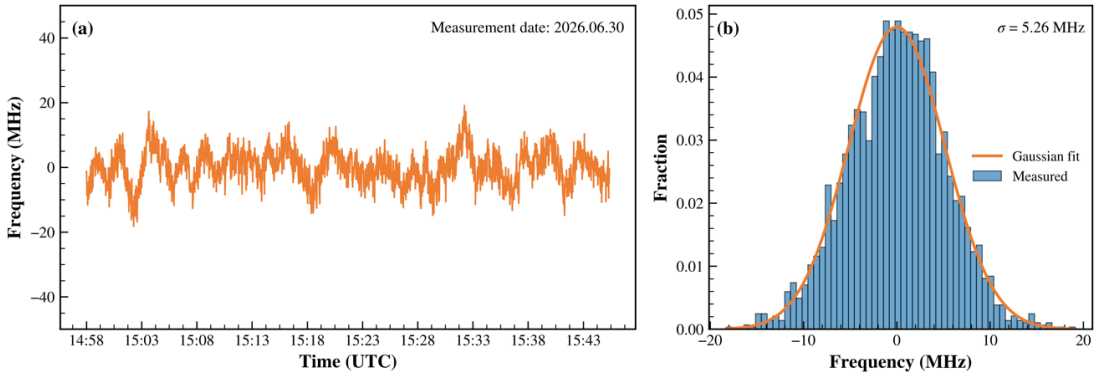


Figure R9. Laser frequency fluctuations measured by a wavelength meter during the atmospheric observation period.

Regarding the optical efficiency listed in Table 1, we would like to clarify that this parameter refers to the overall optical transmission efficiency of the optical components before the received light enters the receiver fiber.

Comment 13)

Table 2: In Table 2 authors specify parameters for the Fabry-Perot etalon. However, it is unclear if this parameters are for the original etalon, or when it is setup to operate in Fizeau interferometer mode. The plates misalignment will affect the peak transmission and the spectral bandwidth. I believe, the “spacer thickness” is more commonly used

terminology than “spacer length”.

Response:

Thank you for this valuable comment. To avoid ambiguity, we have revised Table 2 by replacing the original design parameters of the Fabry–Perot etalon with the corresponding parameters of the Fizeau interferometer used in our lidar system. The revised table now reflects the configuration of the Fizeau interferometer. In addition, we have replaced "spacer length" with "spacer thickness" as suggested by the reviewer. The revised Table 2 is shown here as Table R1.

Table R1. Parameters of the Fizeau interferometer.

Fizeau		
	Peak Transmittance (%)	67
	Spacer Thickness (mm)	12.5
	Mean Plate Reflectivity (%)	≈66
	Measured FWHM (GHz)	2.92
	Measured wedge angle (μrad)	2.83

Comment 14)

Please demonstrate the measured spectra and the fitted RB function convoluted with laser spectrum and receiver transmission spectra for the aerosol free altitude above 5.3 km with robust temperature measurement as a good example of the fit.

Response:

Thank you for this valuable suggestion. To further demonstrate the reliability of our spectral fitting method, we have provided an example of the measured and best-fit spectra at an altitude of 10 km, where the contribution of aerosol scattering is relatively weak.

The measured spectrum was corrected using the experimentally determined illumination function of the 32-channel PMT array. The best-fit spectrum was calculated using our forward model, which accounts for the Rayleigh–Brillouin scattering spectrum, the laser spectral linewidth, and the spectral response of the Fizeau

interferometer.

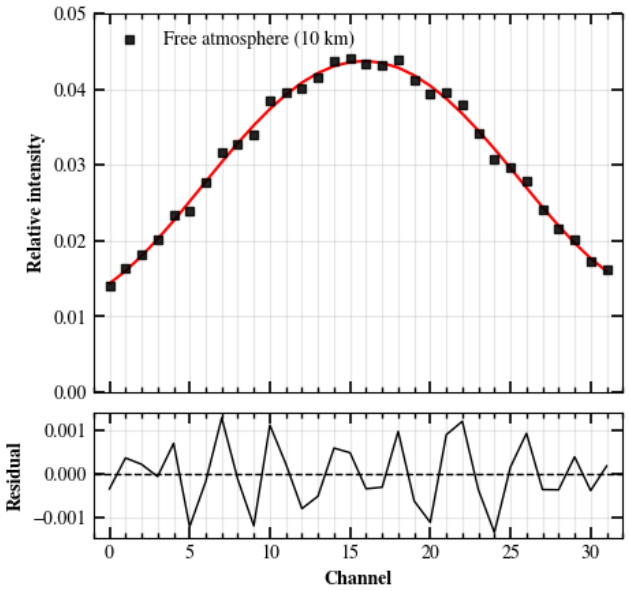


Figure R10. Comparison of the measured spectrum (black squares) and the best-fit spectrum (red solid line) at an altitude of 10 km under free-atmosphere conditions.

As shown in Fig. R10, the fitted spectrum agrees well with the measured spectrum across the detector channels, demonstrating the ability of the proposed retrieval method to reproduce the observed spectral characteristics for the aerosol free altitude.

Comment 15)

Please provide an example with a thin cirrus cloud to demonstrate that Mie scattering signal contamination is entirely confined within the cloud. That will demonstrate how robust the temperature measurements are. The attenuated backscatter profile would be useful for this assessment.

Response:

Thank you for this valuable suggestion. We conducted atmospheric observations under thin-cloud conditions, with a cloud layer located between approximately 8 and 9 km. To characterize the vertical distribution of the cloud layer, we calculated the normalized range-corrected signal profile from the measured photon-counting signals by applying background subtraction and range-squared correction. During the atmospheric measurements, the telescope was tilted at an angle of 15°, which could introduce slight

structural deformation and make it difficult to accurately correct for the geometrical overlap factor. Therefore, to minimize the influence of uncertainties associated with the overlap correction, we present the normalized range-corrected signal profile only above 6 km. The resulting profile is shown in Fig. R11.

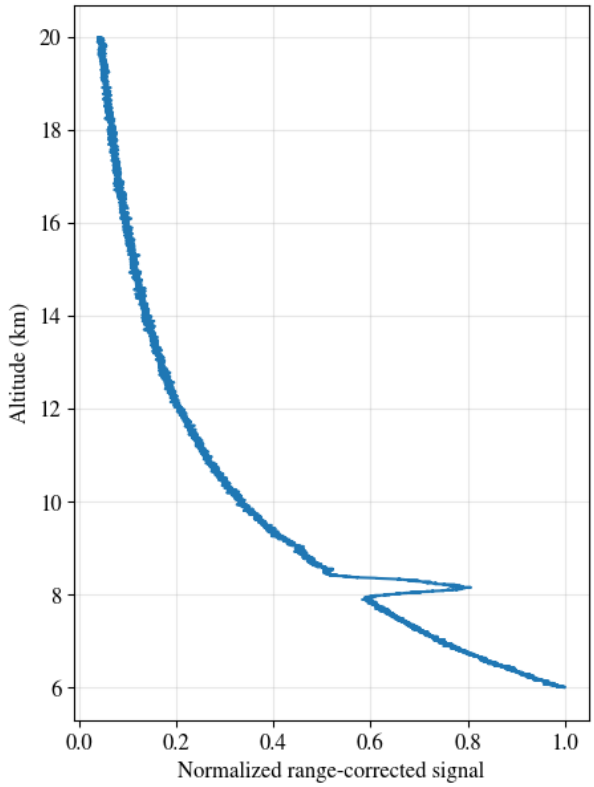


Figure R11. Normalized range-corrected lidar signal derived from the photon counts recorded by the 32-channel PMT array, after background subtraction and range-squared correction, assuming complete transmitter–receiver overlap above 6 km.

However, no radiosonde measurements were available for comparison on that observation day. Nevertheless, we have presented the temperature profile retrieved from the lidar measurements conducted on the same day in Fig. R12.

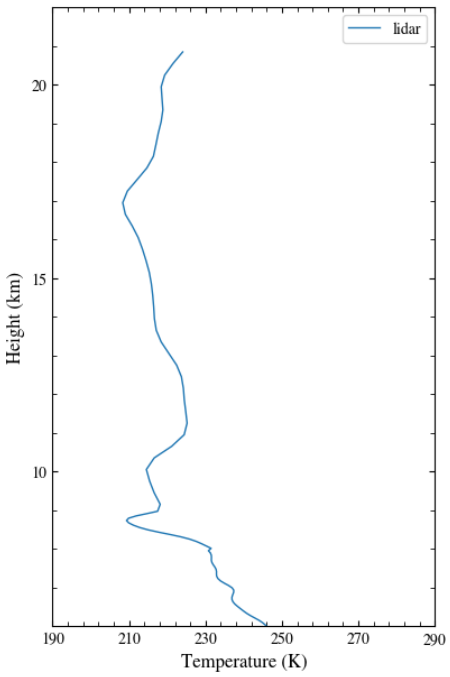


Figure R12. Atmospheric temperature profile retrieved from the lidar measurements under thin-cloud conditions, with a cloud layer located between approximately 8 and 9 km.

As shown in Fig. R12, the retrieved temperature profile exhibits noticeable discontinuities and deviations between 8 and 9 km, where the thin-cloud layer is located. These deviations are likely associated with the enhanced Mie scattering contribution within the cloud layer, which affects the reliability of the temperature retrieval. However, outside this altitude range, the retrieved temperature profile remains relatively continuous and smooth, without significant abrupt changes. This suggests that the influence of Mie scattering contamination on the retrieved temperature profile is primarily confined to the cloud layer, while the temperature retrievals at other altitudes remain relatively stable.

Comment 16)

Please explain if the measured instrument receiver's transmission spectrum measured in the laboratory setting is representative of the receiver transmission spectrum for field operation. Include any adjustments you apply to calibrations to account for the offsets, for example, in detector gain, laser pulse characterization, and indicate if you apply any

range dependent corrections to the receiver's transmission function.

Response:

Thank you for this valuable comment. Regarding the applicability of the laboratory-measured receiver transmission function to atmospheric observations, we would like to clarify that the receiver transmission function was characterized using both a 355 nm continuous-wave laser in the laboratory and the 355 nm pulsed laser employed in the actual lidar system.

Importantly, the pulsed-laser measurements were performed directly on the experimental lidar system. Furthermore, the optical fiber and fiber scrambler used during the calibration measurements were identical to those employed during the atmospheric observations. These arrangements helped minimize differences in optical illumination conditions between the calibration measurements and field operation.

Therefore, the receiver transmission function was characterized under optical conditions closely representative of those used during atmospheric measurements. We have further clarified these experimental arrangements in the revised manuscript (Page 15, Lines 320–325).

Regarding the detector gain correction, we have already addressed this issue in our response to Comment 11.

Regarding the characterization of the pulsed laser spectrum, the spectral response of the Fizeau interferometer was experimentally measured using the same pulsed laser employed during atmospheric measurements. Consequently, the measured spectral response inherently includes the broadening effect of the finite laser linewidth. By directly incorporating this experimentally measured response into the spectral retrieval model, the influence of the pulsed laser linewidth is already accounted for. Therefore, a separate measurement of the pulsed laser linewidth is not required for the retrieval process.

Regarding the laser center frequency, we actively stabilize it using a wavelength meter and monitor the laser wavelength in real time to minimize the impact of center-wavelength variations on wind velocity retrieval.

Regarding the range-dependent correction of the receiver transmission function, a

multimode optical fiber equipped with a mode scrambler was employed in our receiver system to improve the uniformity and stability of the illumination entering the Fizeau interferometer. The mode scrambler promotes mode coupling within the fiber, thereby reducing the sensitivity of the output intensity distribution to variations in the spatial and angular distributions of the atmospheric return signals at different altitudes. This configuration helps minimize range-dependent variations in the illumination conditions of the Fizeau interferometer. Therefore, a common experimentally characterized receiver spectral response was applied throughout the atmospheric retrieval, without introducing an additional range-dependent correction to the transmission function.

Comment 17)

Systematic Error budget: Please, provide an error budget estimate due to instrument hardware limitations: long term laser frequency locking accuracy and frequency drift, laser spectrum stability, interferometer drift, detector gain drift/after pulsing if relevant.

Response:

Thank you for this valuable comment. We appreciate the reviewer's suggestion to provide a more comprehensive assessment of the systematic uncertainties associated with the hardware performance of our lidar system. We agree that evaluating the influence of instrument stability and potential systematic errors is important for assessing the reliability of the retrieved atmospheric temperature and wind profiles. In response to this comment, we have further examined the relevant instrumental factors and provide detailed explanations below.

Regarding the laser frequency stability, we monitored the frequency fluctuations of the 355 nm pulsed laser using a HighFinesse WS8-2 wavelength meter. The measurement was conducted on 30 June 2026, and the results are presented in Fig. R9. The laser frequency remained relatively stable throughout the approximately 46-minute measurement period, without exhibiting a significant systematic drift. These results also demonstrate the effectiveness of the laser frequency-locking system in maintaining frequency stability during operation. The statistical distribution of the frequency fluctuations is shown in Fig. R9(b), with a standard deviation of 5.26 MHz which

corresponds to an equivalent line-of-sight velocity fluctuation of approximately 0.93 m s^{-1}. Importantly, during atmospheric observations, the transmitted laser frequency was continuously monitored using the wavelength meter, providing a real-time frequency reference for the Doppler wind retrieval. The recorded frequency variations can therefore be used to correct the frequency reference and reduce the influence of laser frequency fluctuations on the retrieved wind velocities. Furthermore, our lidar system determines the horizontal wind components from Doppler measurements performed in opposite viewing directions. By taking the difference between the Doppler velocities measured in opposite directions, common systematic frequency offsets can be largely cancelled, further reducing their influence on the retrieved wind profiles.

Regarding the laser spectral stability, before each atmospheric measurement, the spectral transmission response of the Fizeau interferometer was experimentally characterized using the same pulsed laser employed for atmospheric observations. The measured spectral response inherently includes the combined effects of variations in the laser spectral characteristics, potential drift of the Fizeau interferometer, and changes in the relative responses of individual channels of the linear PMT array. Therefore, comparing the spectral response curves obtained before different atmospheric measurements allows us to evaluate the overall stability of the receiver system. The corresponding experimental results are presented in Figure R13, showing good consistency among the independently measured spectral response curves. These results indicate that the combined effects of these potential instrumental variations were relatively small during the measurement periods.

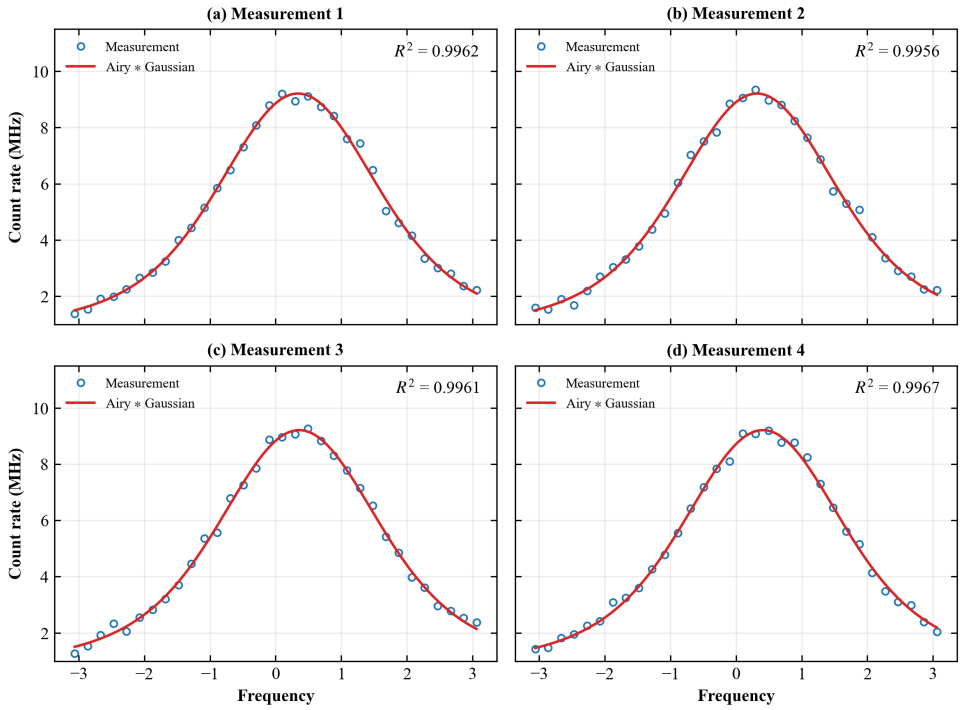


Figure R13. Receiver calibration results.

The four calibration measurements yielded a sample standard deviation of 12.3 MHz in the FWHM of the combined laser–Fizeau response, corresponding to approximately 0.40% of its mean spectral width. To assess the impact on temperature retrieval, the fitted responses were convolved with Rayleigh–Brillouin scattering spectra using the Witschas analytical model (Witschas, 2011a, b). For temperatures of 210–260 K and standard atmospheric pressures corresponding to altitudes of 2–20 km, the variability among these four calibrations produced a standard deviation of approximately 1.08–1.26 K in the retrieved temperatures.

Regarding the drift of the Fizeau interferometer, we analyzed the frequency-to-channel response to Doppler frequency shifts through six independent frequency-scanning calibration measurements. The mean calibration slope across the six measurements was 197.53 MHz/channel, with a relative slope variation (expressed as the relative standard deviation) of approximately 0.96%, indicating good repeatability of the Doppler frequency-shift response calibration under the tested conditions. The corresponding contribution to the wind-speed uncertainty is estimated to be approximately 0.19 m s^{-1} for a line-of-sight wind speed of 20 m s^{-1} (Pages 16, Lines 334–358). The added Fig. 9

is shown here as Fig. R14.

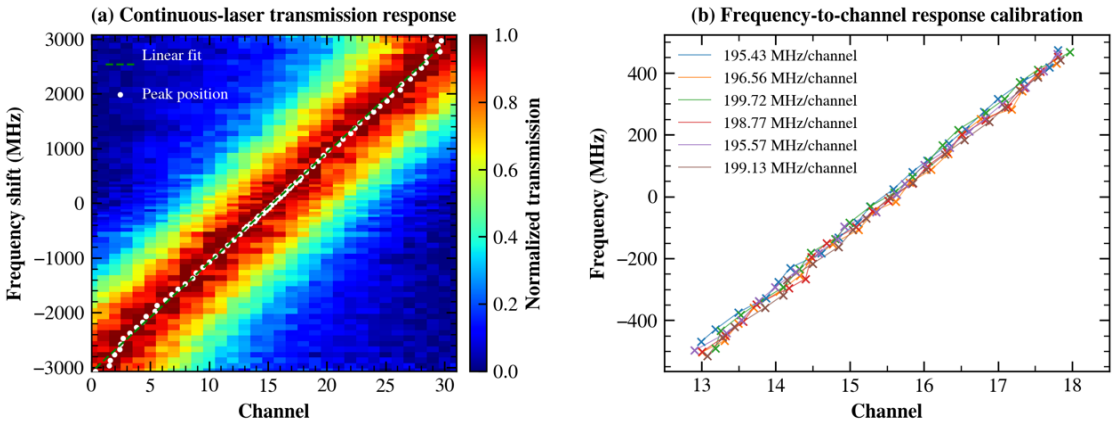


Figure R14. Calibration of the frequency-to-channel response. (a) Measured continuous-wave laser transmission response as a function of detector channel and laser frequency shift. The white dots indicate the fitted peak positions, and the dashed line represents the corresponding linear fit. (b) Frequency-to-channel response obtained from six independent frequency-scanning measurements, with the fitted slopes indicated in the legend.

Regarding the detector gain drift, the relative response differences among the 32 detector channels have been corrected using the illumination function. During atmospheric measurements, the photon-counting acquisition system operated with a dead time of 2 ns. To account for potential counting losses at high photon count rates, a dead-time correction can be applied to the measured photon counts based on the non-paralyzable detector model.

$$R_{corrected} = \frac{R_{measured}}{1 - R_{measured}\tau}$$

where $R_{corrected}$ represents the corrected photon count rate, $R_{measured}$ denotes the photon count rate recorded by the acquisition system, and τ is the dead time of the photon-counting system. This correction compensates for the underestimation of photon counts caused by the finite dead time of the acquisition system.

Furthermore, the receiver calibration inherently includes the combined effects of potential detector response drift, variations in the laser spectral characteristics, and drift of the Fizeau interferometer. Therefore, the influence of detector response variations is already reflected in the repeatability of the experimentally measured receiver response. The potential contribution of these combined instrumental variations to the wind-speed

uncertainty has been analyzed above.

The H11460-200 detector employs an ultra-bialkali (UBA) photocathode and a metal-channel dynode structure and is operated within the manufacturer's recommended operating limits. Förtsch et al. investigated 1100 Hamamatsu H12700 metal-channel multi-anode PMTs and reported a mean afterpulse probability of 0.93% (Förtsch et al., 2026). Dinoev et al. reported that Hamamatsu metal-channel photomultiplier tubes exhibited negligible signal-induced noise (SIN) under the right operating conditions (Dinoev et al., 2013). Therefore, we expect the influence of afterpulse on our lidar measurements to be relatively small and unlikely to represent a dominant source of retrieval uncertainty under our operating conditions.

Comment 18)

Indicate if the measurements can be performed during day time or are limited only to the night operation.

Response:

Thank you for this comment. At present, daytime measurements have not yet been conducted using our lidar system.

Comment 19)

Fig 2(a): The presented conceptual image lacks clear labeling, "faint" fiber connection. Please consider replacing this conceptual 3D image with a 2D optical schematics. Also, consider to use a presentation style similar to Xia et al., "Stratospheric temperature measurement with scanning Fabry-Perot interferometer for wind retrieval from mobile Rayleigh Doppler lidar," Optics Express, 22, 21775–21789 (2014). I believe this paper describes the same instrument.

Response:

Thank you for this valuable suggestion. We have revised Fig. 2 by replacing the original 3D optical layout with a clearer 2D optical schematic to better illustrate the optical configuration and light paths of the lidar system.

Comment 20)

Fig 2(b): The photograph appears to be not informative. I suggest replacing it with 2D schematics of the Fizeau optical layout or use a semitransparent 3D CAD rendering. Please use font colors with higher contrast for labels.

Response:

Thank you for this valuable suggestion. We have retained the original photograph in Fig. 2(b) and added a 3D CAD schematic of the receiver to provide a clearer illustration of its internal optical configuration and component arrangement. In addition, we have used higher-contrast font colors for the labels to improve their visibility and readability.

Comment 21)

Fig 2(c): The photograph is not informative and appears to show a black shipping container. Please consider replacing it with an image of the actual instrument or semitransparent 3D CAD rendering.

Response:

Thank you for this valuable suggestion. We have replaced the original photograph of the USTC Doppler wind lidar in Fig. 2(c) with a 3D rendering to provide a clearer and more informative representation of the instrument's overall structure. The revised Fig. 2 is shown here as Fig. R15.

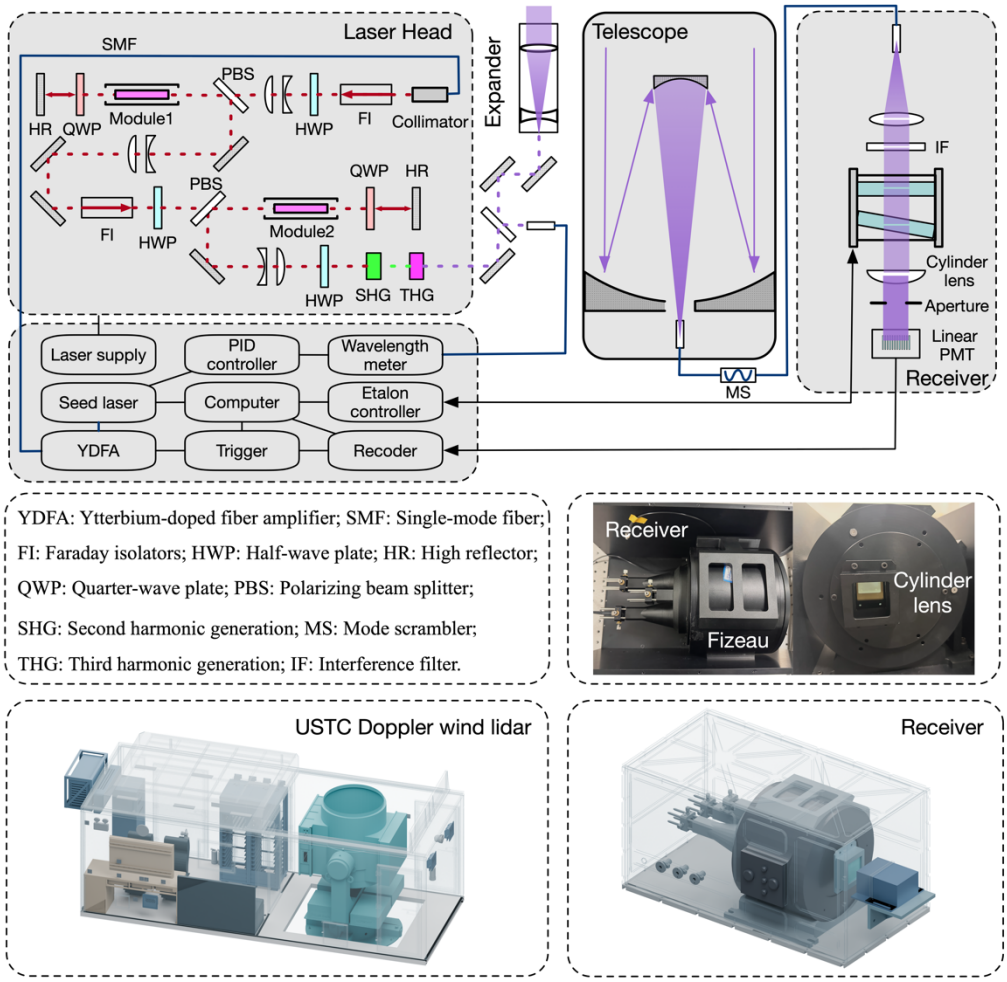


Figure R15. Schematic of the developed HSRL system.

Comment 22)

Line 193: Please replace “fineness” with “finesse” throughout the manuscript, including the tables.

Response:

Thank you for pointing out this terminology error. We have replaced "fineness" with "finesse" as suggested. The corresponding corrections have been made on Page 5, Line 143.

Comment 23)

Line 320: Please replace “Mie scattering energy” with “Mie scattering signal” for consistency with the terminology.

Response:

Thank you for pointing out this terminology issue. We have replaced "Mie scattering energy" with "Mie scattering signal" in the revised manuscript, as suggested by the reviewer. The corresponding corrections have been made on Page 1, Lines 24; Page 4, Line 117; and Page 18, Line 370**.**

Comment 24)

Throughout the manuscript: The authors report simulated temperature and wind retrieval error with two decimal places. This may be confused with the measurement accuracy of the instrument. Please reconsider how you report the results of these simulations to make it consistent with the error estimates.

Response:

Thank you for this valuable suggestion. We have revised the numerical precision of the simulated temperature and wind retrieval errors throughout the manuscript to avoid confusion with the actual measurement accuracy of the lidar system.

References in this response:

Dinoev, T., Simeonov, V., Arshinov, Y., Bobrovnikov, S., Ristori, P., Calpini, B., Parlange, M., and van den Bergh, H.: Raman Lidar for Meteorological Observations, RALMO – Part 1: Instrument description, Atmospheric Measurement Techniques, 6, 1329-1346, 10.5194/amt-6-1329-2013, 2013.

Förtsch, J., Kampert, K. H., Patel, V., Pauly, C., and Pfeifer, D.: Series testing and characterization of 1100 Hamamatsu H12700 Multianode Photomultiplier tubes, Nuclear Instruments and Methods in Physics Research Section A: Accelerators, Spectrometers, Detectors and Associated Equipment, 1083, 171147, https://doi.org/10.1016/j.nima.2025.171147, 2026.

Hagen, N., Kupinski, M., and Dereniak, E. L.: Gaussian profile estimation in one dimension, Applied Optics, 46, 5374-5383, 10.1364/AO.46.005374, 2007.

Witschas, B.: Analytical model for Rayleigh–Brillouin line shapes in air, Applied Optics, 50, 267-270, 10.1364/AO.50.000267, 2011a.

Witschas, B.: Analytical model for Rayleigh–Brillouin line shapes in air: errata, Applied Optics, 50, 5758-5758, 10.1364/AO.50.005758, 2011b.